

Supplementary Information

Interlinked multiphase Fe-doped MnO₂ nanostructures: a novel design for enhanced pseudocapacitive performance

Ziya Wang,^a Fengping Wang,^{*a} Yan Li,^a Jianlin Hu,^a Yanzhen Lu^a and Mei Xu^a

Department of Physics, School of Mathematics and Physics, University of Science and Technology Beijing, Beijing, PR China

Corresponding author: fpwang@ustb.edu.cn (F. Wang)

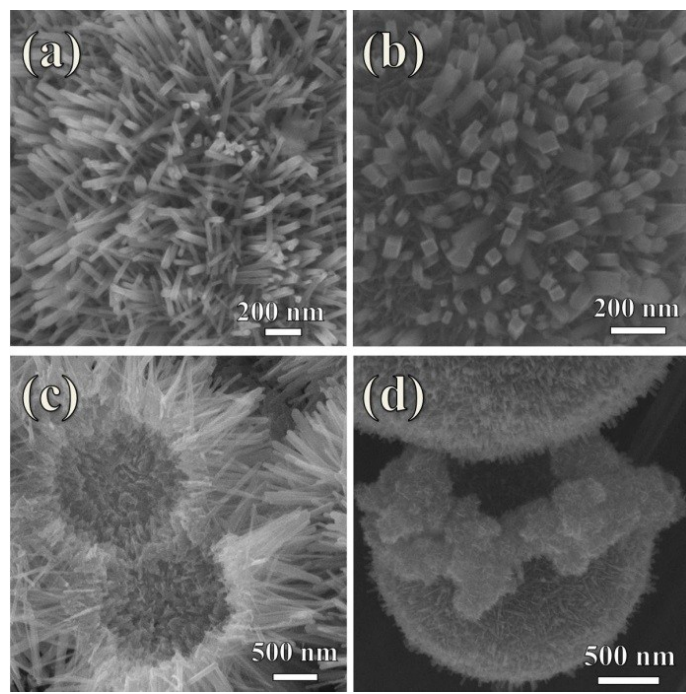


Fig. S1 the nanorods growing on the surface of (a) $\text{MnO}_2\text{-1/8}$ and (b) $\text{MnO}_2\text{-1/4}$ microspheres; the broken parts of (c) $\text{MnO}_2\text{-1/8}$ and (d) $\text{MnO}_2\text{-1/4}$ hollow microspheres.

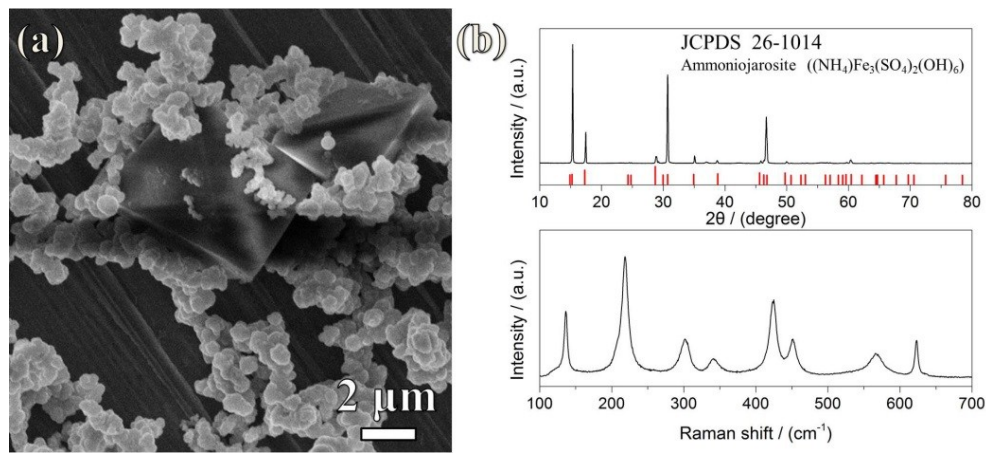


Fig. S2 (a) SEM image of $\text{MnO}_2\text{-2/1}$; (b) XRD pattern and Raman spectrum of $\text{MnO}_2\text{-2/1}$, indicating that the huge crystals are ammoniojarosite $((\text{NH}_4)\text{Fe}_3(\text{SO}_4)_2(\text{OH})_6)$, (JCPDS 26-1014).

Table S1 The weight percent of O, Mn and Fe atoms.

| Sample \ Element | O | Mn | Fe |
|------------------------|--------|--------|--------|
| Sample | O | Mn | Fe |
| MnO ₂ -0 | 28.22% | 71.78% | \ |
| MnO ₂ -1/16 | 29.06% | 67.24% | 3.7% |
| MnO ₂ -1/8 | 28.34% | 64.78% | 6.88% |
| MnO ₂ -1/4 | 27.34% | 61.77% | 10.89% |
| MnO ₂ -1/2 | 27.78% | 52.68% | 19.54% |
| MnO ₂ -1/1 | 28.83% | 42.76% | 28.41% |
| MnO ₂ -2/1 | 26.90% | 43.17% | 29.93% |

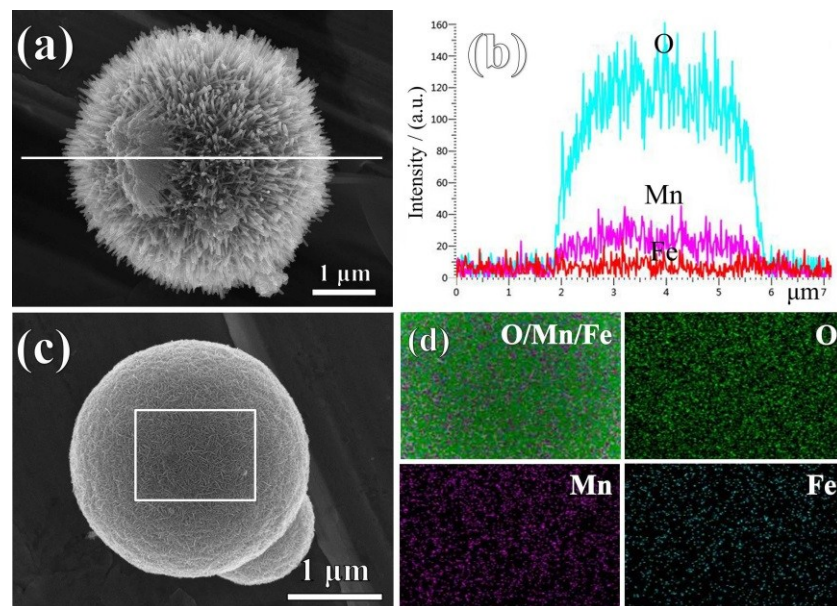


Fig. S3 (a-b) EDS line scanning of MnO₂-1/8; (c-d) EDS mapping scanning of MnO₂-1/2, demonstrating that the O, Mn and Fe elements are uniformly distributed in the microsphere.

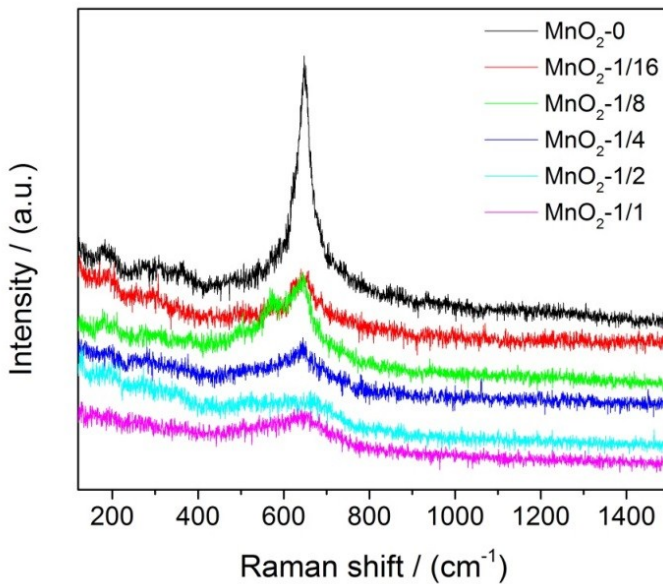


Fig. S4 Raman spectra of MnO₂-0 to MnO₂-1/1.

Description of Fig. S4:

To further verify the structure and composition of Fe-doped MnO₂, Raman spectroscopy was conducted. It is seen that the strongest Raman band at 647 cm⁻¹ for MnO₂-0 is in good agreement with the symmetric stretching vibration ν_2 (Mn-O) of α -MnO₂.^{1, 2} With increasing Fe doping concentration, the peak shifts to lower wavenumbers with sharply degraded intensity, which is indicative of a poorer crystallinity and substitution (or insertion) of Fe³⁺. Specially, MnO₂-1/8 shows the evident peak of about 570 cm⁻¹, which is the specific fingerprint of the Mn-O vibration along the chains in the manganese dioxide framework. This mode appears at 570 cm⁻¹ in R-MnO₂.³

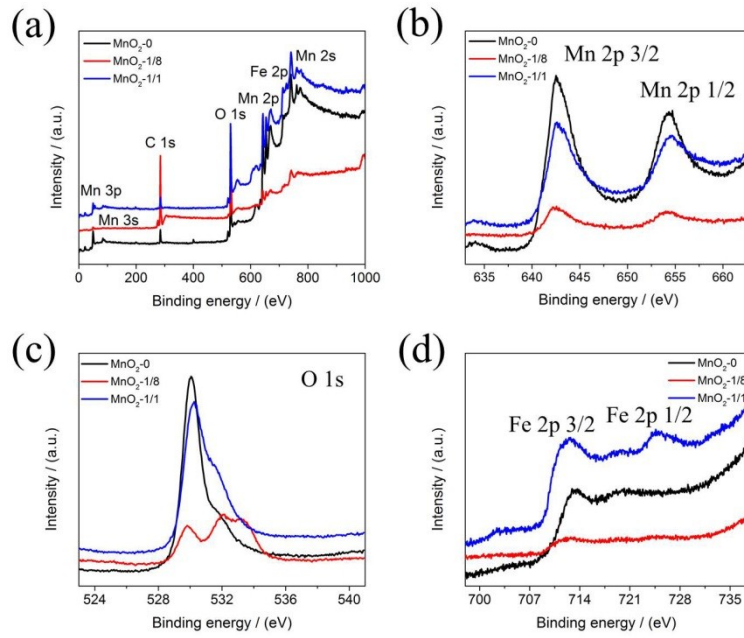


Fig. S5 (a) XPS survey spectra and high resolution XPS spectra of (b) Mn 2p, (c) O 1s, and (d) Fe 2p peaks for the MnO₂-0, MnO₂-1/8 and MnO₂-1/1, respectively.

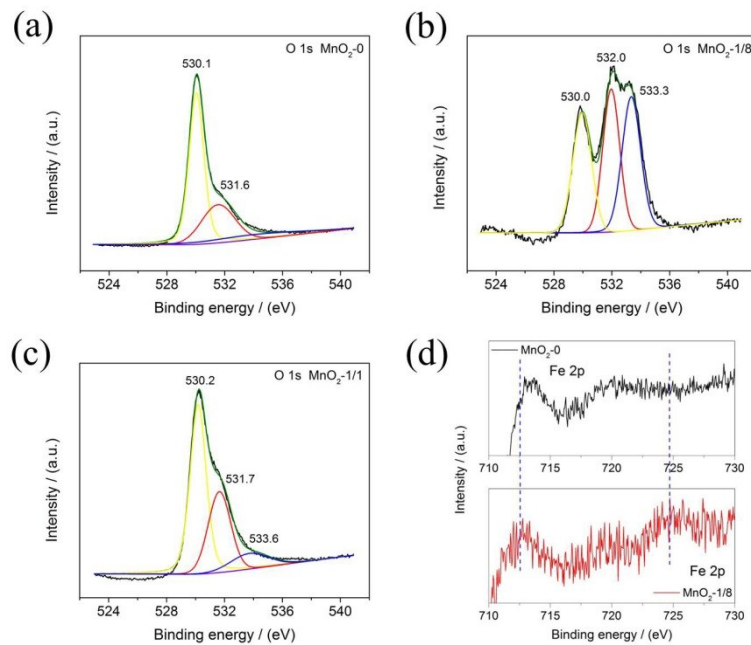


Fig. S6 High-resolution core level O 1s XPS spectra of (a) MnO₂-0, (b) MnO₂-1/8 and (c) MnO₂-1/1; (d) the magnified view of Fe 2p XPS spectra of MnO₂-0, and MnO₂-1/8, respectively. It shows that no peak of Fe 2p in the MnO₂-0.

Description of Fig. S5 and Fig. S6:

Fig. S5 illustrates the chemical composition and metal oxidation states of the representative samples. For the Mn 2p spectra (Fig. S5(b)), the binding energy separation between core level Mn 2p 1/2 (654.3 eV) and Mn 2p 3/2 (642.7 eV) is ~11.6 eV, which matches with the dominant Mn(IV) oxidation state.⁴ In the O 1s spectra (Fig. S5(c) and Fig. S6(a-c)), the peaks of MnO₂-0 at 530.1 and 531.6 eV are related to the metal-oxygen bond (Mn-O)⁵ and adsorbed oxygen in OH⁻ groups (Mn-O-H),⁶ respectively. For the Fe-doped MnO₂ samples, the two peak positions remain nearly unchanged. A new peak appeared at 533.3 eV can be attributed to multiplicity of physi- and chemi-sorbed water at or near the surface (H-O-H).⁷ Interestingly, MnO₂-1/8 shows two relatively strong peaks at 532.0 eV and 533.3 eV, respectively. This could be because of its special three phases interconnected structure. Moreover, the Fe 2p spectra observed in the Fe-doped samples manifest the successful doping (Fig. S5(d) and Fig. S6(d)). Two peaks at 724.3 and 712.4 eV are assigned to Fe³⁺ (2p 1/2) and Fe³⁺ (2p 3/2), respectively.⁸

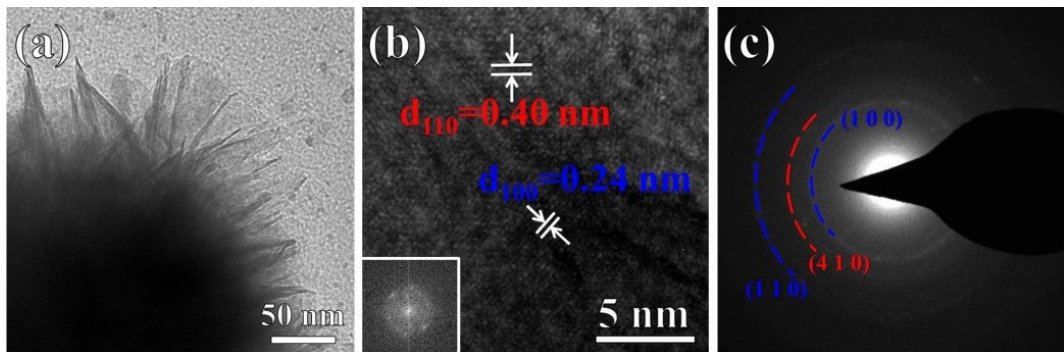


Fig. S7 (a) TEM image, (b) HRTEM image and (c) SAED pattern of MnO₂-1/1. (the red and blue words stand for the R-MnO₂ phase and ε-MnO₂ phase, respectively.)

Table S2 Parameters for BET surface area and pore volume of MnO₂-0 to MnO₂-1/1.

| Sample | BET surface area / (m ² g ⁻¹) | Pore volume / (cm ³ g ⁻¹) |
|------------------------|--|--|
| MnO ₂ -0 | 106.668 | 0.219 |
| MnO ₂ -1/16 | 114.844 | \ |
| MnO ₂ -1/8 | 146.666 | 0.397 |
| MnO ₂ -1/4 | 174.253 | \ |
| MnO ₂ -1/2 | 263.084 | \ |
| MnO ₂ -1/1 | 300.484 | 0.322 |

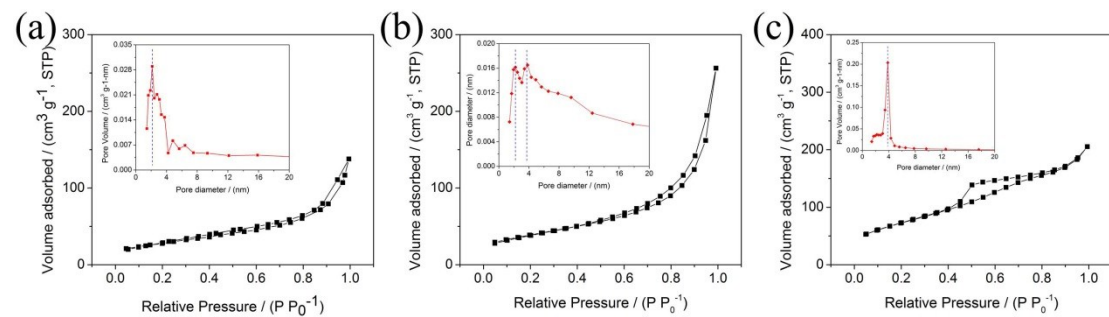


Fig. S8 Nitrogen adsorption-desorption isotherms and pore size distribution curves of (a) MnO₂-0, (b) MnO₂-1/8 and (c) MnO₂-1/1, respectively. Both MnO₂-1/8 and MnO₂-1/1 show the increased specific surface area compared with MnO₂-0. Although the specific surface area of MnO₂-1/8 is smaller than that of MnO₂-1/1, the pore volume and the larger mesopore ratio of MnO₂-1/8 are advantageous in rate capability.

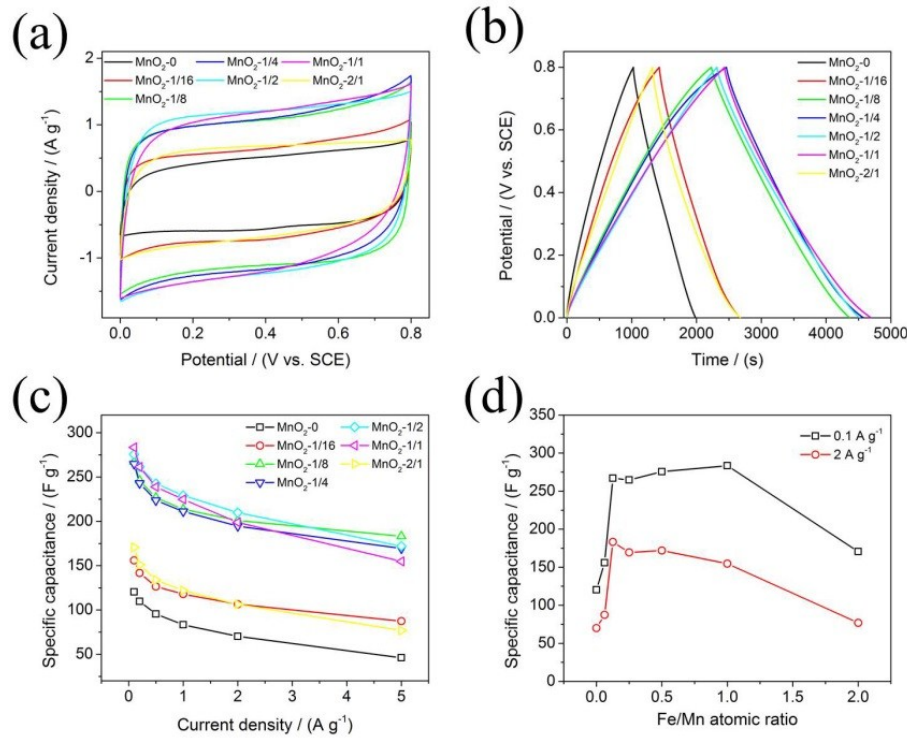


Fig. S9 (a) CV and (b) GCD curves of MnO₂-0 to MnO₂-2/1 under the similar mass loading of ~5 mg at 5 mV s⁻¹ and 0.1 A g⁻¹, respectively; (c) Gravimetric capacitance as a function of current density for MnO₂-0 to MnO₂-2/1; (d) Plot of the specific capacitances of the products versus Fe/Mn atomic ratios at 0.1 A g⁻¹ and 2 A g⁻¹, respectively. In the pictures of (c-d), Fe-doped MnO₂ shows a further depression at high current density from MnO₂-1/2 with the increasing of dopant concentration.

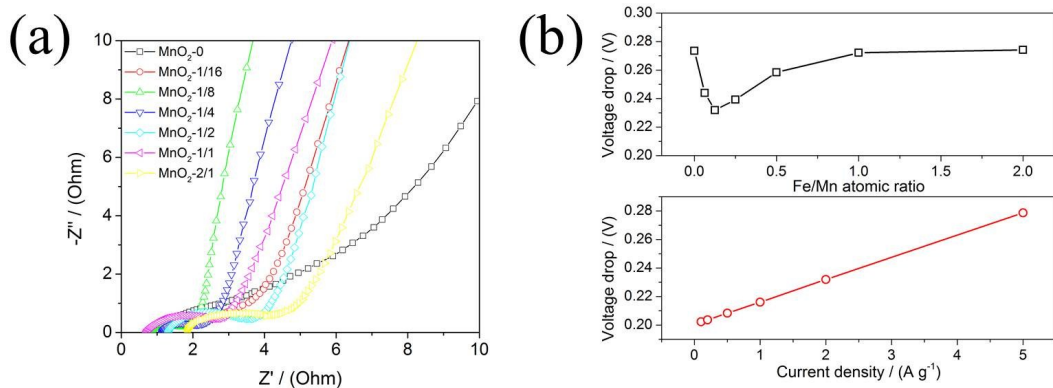


Fig. S10 (a) Nyquist plots of MnO₂-0 to MnO₂-2/1 by applying an AC voltage of 5 mV amplitude at 0.01 Hz to 100 kHz. The fitted impedance parameters are listed in

Table S1. (b) Image above: IR drop versus Fe/Mn atomic ratios at 1 A g⁻¹; Image below: IR drop of the MnO₂-1/8 supercapacitor at different current densities.

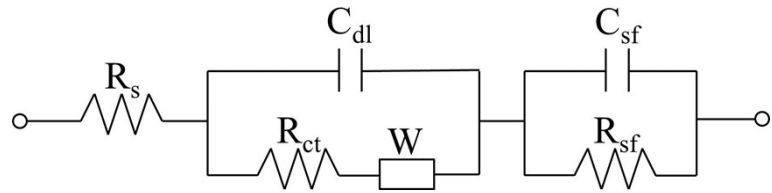


Fig. S11 (a) equivalent electric circuit used for EIS data fitting (R_s : combined series resistance; R_{ct} : charge-transfer resistance; W : Warburg element; C_{dl} : electrical-double-layer capacitance; C_{sf} : pseudo-capacitance; R_{sf} : surface resistance).

Table S3 Parameters of equivalent circuit elements.

| electrode | $R_s / (\Omega)$ | $R_{ct} / (\Omega)$ |
|------------------------|------------------|---------------------|
| MnO ₂ -0 | 1.296 | 3.432 |
| MnO ₂ -1/16 | 1.336 | 1.927 |
| MnO ₂ -1/8 | 0.989 | 0.665 |
| MnO ₂ -1/4 | 1.274 | 0.796 |
| MnO ₂ -1/2 | 1.474 | 2.213 |
| MnO ₂ -1/1 | 0.982 | 2.118 |
| MnO ₂ -2/1 | 2.034 | 2.844 |

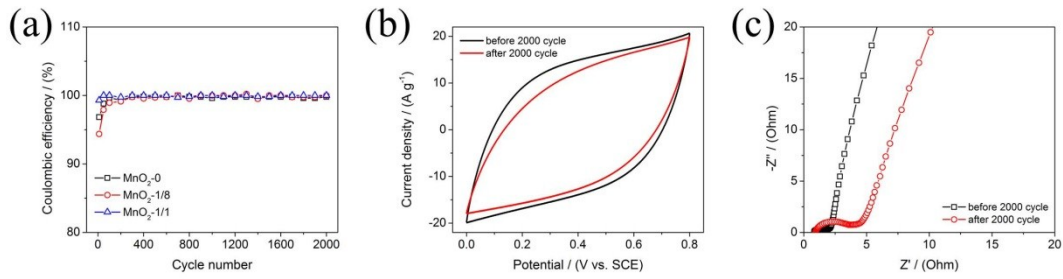


Fig. S12 (a) Coulombic efficiency (nearly 100%) of MnO₂-0, MnO₂-1/8 and MnO₂-1/1 at a current rate of 2 A g⁻¹; (b) the cyclic voltammetry curves and (c) Nyquist plots of MnO₂-1/8 collected before and after 2000 cycles. The MnO₂-1/8 electrode are highly conductive with small electrochemical impedance values. After 2000 cycles, the impedance values increase but still acceptably low.

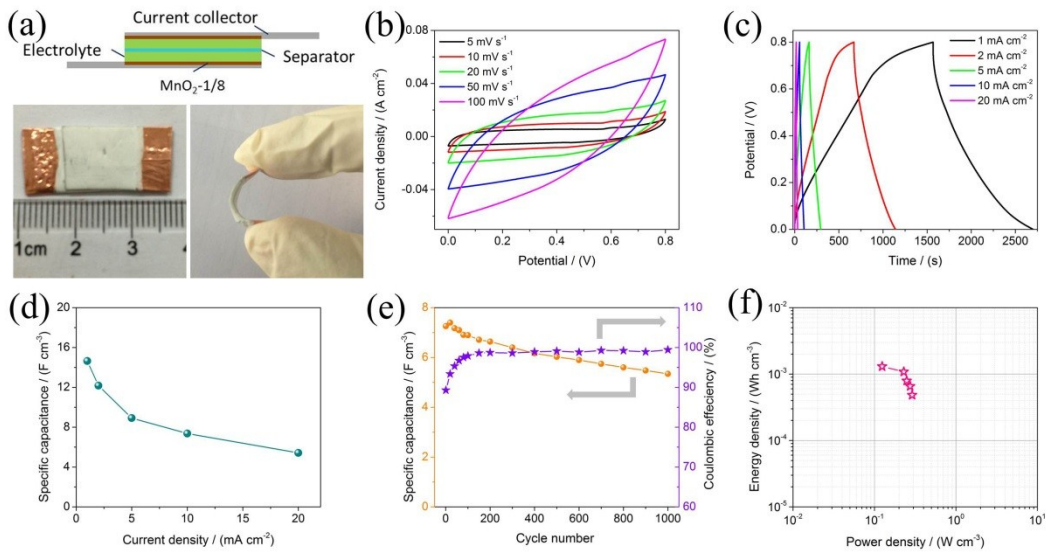


Fig. S13 (a) Schematic illustration and digital images, (b) CV curves, (c) GCD curves, (d) rate capability, (e) cycling performance and (f) Ragone plot of the all-solid-state SSC device.

Table S4 Electrochemical performance of selected metal doped MnO₂ materials for supercapacitors

| item | electrolyte | mass loading | specific capacitance | Cycling stability | ref |
|---|---------------------------------------|----------------------------------|--|--|-----------|
| Fe-doped MnO ₂ (α -/R-/ ε -) | 1 M Na ₂ SO ₄ | 5 mg cm ⁻¹ | 213.5 F g ⁻¹ at 1 A g ⁻¹ 366.6 F g ⁻¹ at 20 mV s ⁻¹ | 100 % after 2000 cycles at 2 A g ⁻¹ | This work |
| α -MnO ₂ | 1 M Na ₂ SO ₄ | 0.5 mg cm ⁻¹ | \sim 290 F g ⁻¹ at 20 mV s ⁻¹ | 66 % after 500 cycles at 1 A g ⁻¹ | 9 |
| Fe-doped ε -MnO ₂ | 1 M Na ₂ SO ₄ | 0.2 mg cm ⁻¹ | 120 F g ⁻¹ at 5 mV s ⁻¹ | \ | 10 |
| Na-doped cryptomelane MnO ₂ | 0.5 M Na ₂ SO ₄ | 0.5 mg cm ⁻¹ | 153.7 F g ⁻¹ at 25 mV s ⁻¹ | \ | 11 |
| Al-doped α -MnO ₂ | 1 M Na ₂ SO ₄ | 0.2 mg cm ⁻¹ | 100 F g ⁻¹ at 5 mV s ⁻¹ | \ | 10 |
| Al-doped α -MnO ₂ | 1 M Na ₂ SO ₄ | 4 mg | \sim 130 F g ⁻¹ at 1 A g ⁻¹ | 91 % after 15000 cycles at 2 A g ⁻¹ | 12 |
| Co-doped R-MnO ₂ | 1 M Na ₂ SO ₄ | \ | 146 F g ⁻¹ at 20 mV s ⁻¹ | 90 % after 1000 cycles at 2 A g ⁻¹ | 13 |
| Co-doped α -MnO ₂ | 1 M Na ₂ SO ₄ | \sim 0.6 mg cm ⁻¹ | 250 F g ⁻¹ at 1 A g ⁻¹ | 97.3% after 5000 cycles at 5 A g ⁻¹ | 14 |
| Zn-doped δ -MnO ₂ | 0.5 M Na ₂ SO ₄ | \sim 5 mg cm ⁻¹ | \sim 120 F g ⁻¹ at 20 mV s ⁻¹ | \sim 73% after 1000 cycles at 0.05 A g ⁻¹ | 15 |
| Zn-doped α -MnO ₂ | 0.5 M KCl | < 0.5 mg cm ⁻¹ | \sim 440 F g ⁻¹ at 20 mV s ⁻¹ | \ | 16 |
| Mo-doped MnO ₂ | 0.5 M Na ₂ SO ₄ | \ | 175.5 F g ⁻¹ at 20 mV s ⁻¹ | \ | 17 |
| Ag-doped MnO ₂ | 1 M Na ₂ SO ₄ | \ | 208 F g ⁻¹ at 20 mV s ⁻¹ | \ | 18 |
| Au-doped spinel MnO ₂ | 2 M Li ₂ SO ₄ | \sim 0.025 mg cm ⁻¹ | \sim 530 F g ⁻¹ at 20 mV s ⁻¹ | 93 % after 15000 cycles at 50 mV s ⁻¹ | 19 |

Description of Table S4:

It is worth noting that several different metrics were used to calculate the capacitance and cycling stability in the literature. Because the mass loading of electrodes were not factored in these calculations, the reported values of specific capacitance were often overestimated, thus leading to unrealistic claims, especially for some low mass loading materials.

References

1. H. Wang, F. Yin, B. Chen and G. Li, *J. Mater. Chem. A*, 2015, **3**, 16168-16176.
2. F. Buciuman, F. Patcas, R. Craciun and D. R. T. Zahn, *Phys. Chem. Chem. Phys.*, 1999, **1**, 185-190.
3. C. Julien, M. Massot, R. Baddour-Hadjean, S. Franger, S. Bach and J. P. Pereira-Ramos, *Solid State Ionics*, 2003, **159**, 345-356.
4. Z. Jian, S. Tang, X. Hao, Y. Dai and X. Meng, *ACS Appl. Mater. Inter.*, 2014, **6**, 17637-17646.
5. B. Babakhani and D. G. Ivey, *J. Power Sources*, 2010, **195**, 2110-2117.
6. D. Crihan, M. Knapp, S. Zweidinger, E. Lundgren, C. J. Weststrate, J. N. Andersen, A. P. Seitsonen and H. Over, *Angew. Chem.*, 2008, **120**, 2161-2164.
7. C. Yuan, J. Li, L. Hou, X. Zhang, L. Shen and X. W. D. Lou, *Adv. Funct. Mater.*, 2012, **22**, 4592-4597.
8. J. Liu, Z. Zhao, P. Shao and F. Cui, *Chem. Eng. J.*, 2015, **262**, 854-861.
9. S. Devaraj and N. Munichandraiah, *J. Electrochem. Soc.*, 2007, **154**, A80-A88.
10. P. Yu, X. Zhang, D. Wang, L. Wang and Y. Ma, *Cryst. Growth Des.*, 2009, **9**, 528-533.
11. T. M. Ou, C. T. Hsu and C. C. Hu, *J. Electrochem. Soc.*, 2015, **162**, A5124-A5132.
12. Z. Hu, X. Xiao, C. Chen, T. Li, L. Huang, C. Zhang, J. Su, L. Miao, J. Jiang and Y. Zhang, *Nano Energy*, 2015, **11**, 226-234.
13. C. L. Tang, X. Wei, Y. M. Jiang, X. Y. Wu, L. N. Han, K. X. Wang and J. S. Chen, *J. Phys. Chem. C*, 2015, **119**, 8465-8471.
14. B. C. Kim, C. Justin Raj, W. J. Cho, W. G. Lee, H. T. Jeong and K. H. Yu, *J. Alloy Compd.*, 2014, **617**, 491-497.
15. J. W. Wang, Y. Chen and B. Z. Chen, *Met. Mater. Int.*, 2014, **20**, 989-996.
16. R. Poonguzhalai, N. Shanmugam, R. Gobi, A. Senthilkumar, R. Shanmugam and K. Sathishkumar, *RSC Adv.*, 2015, **5**, 45407-45415.
17. M. Nakayama, A. Tanaka, Y. Sato, T. Tonosaki and K. Ogura, *Langmuir*, 2005, **21**, 5907-5913.
18. G. Zhang, L. Zheng, M. Zhang, S. Guo, Z. H. Liu, Z. Yang and Z. Wang, *Energ. Fuel.*, 2011, **26**,

618-623.

19. J. Kang, A. Hirata, L. Kang, X. Zhang, Y. Hou, L. Chen, C. Li, T. Fujita, K. Akagi and M. Chen, *Angew. Chem. Int. Edit.*, 2013, **52**, 1664-1667.